Nanoscale photocurrent mapping in perovskite solar cells

Yohan Yoon[a,b,1,*], Dongheon Ha[a,b,1,*], Ik Jae Park[c], Paul M. Haney[a], Sangwook Lee[d], Nikolai B. Zhitenev[a]

[a]Center for Nanoscale Science and Technology, National Institute of Standards and Technology, Gaithersburg, Maryland 20899, United States
[b]Maryland Nanocenter, University of Maryland, College Park, Maryland 20742, United States
[c]Department of Materials Science and Engineering, Seoul National University, Seoul 151-742, Korea
[d]School of Materials Science and Engineering, Kyungpook National University, Daegu 41566, Korea

ABSTRACT

In this work, we study spatially-resolved generation of photocurrent of methylammonium lead iodide ($CH_3NH_3PbI_3$) perovskite solar cells to reveal the microscopic effects of annealing temperature and material degradation under light exposure. Correlating a novel nanoscale near-field scanning photocurrent microscopy (NSPM) technique with X-ray diffraction and electron microscopy data, we found that the segregation of lead iodide (PbI_2) driven either by a temperature treatment or by extended light exposure can impact the photocurrent at grain boundaries. In samples annealed at a moderate temperature (100 °C), a small amount of expelled PbI_2 passivates the grain boundaries and improves photocurrent generation. A higher annealing temperature (130 °C) causes further segregation of PbI_2 at grain boundaries, decreasing the photocurrent. Extended light illumination drives further material segregation, decreasing photocurrent both at grain boundaries and grain interiors.

KEYWORDS

Near-field scanning optical microscopy (NSOM), Perovskite, Nanoscale photocurrent, Lead iodide (PbI_2), Light-induced degradation, Degradation mechanism

1. Introduction

Organometal trihalide perovskites show great promise for solar energy harvesting due to their easy fabrication, low manufacturing costs, and high-power conversion efficiencies, now exceeding 22 % [1,2]. Beyond photovoltaics (PVs), the bandgap tunability of perovskites [3-5] enables a wider array of other optoelectronic applications such as light emitting diodes [6,7] and photodetectors [8-10]. To date, considerable efforts have been made to reveal the recombination mechanisms limiting perovskite solar cells' performance [11-14]. Despite the remarkable progress in the cell performance, some aspects of the material inhomogeneity such as its relation to processing conditions and its impact on the carrier recombination processes are not well established. For example, the role of grain boundaries (GBs) in the overall performance of the cell is still largely controversial with reports finding increased losses [15-17] or improved efficiency [18-23] from GBs. Furthermore, perovskite solar cells have reliability issues, especially light-induced degradation [24-27], which are often driven by or related to changes in the microstructure [16].

The techniques for measuring spatially-resolved photoelectric properties such as local carrier collection efficiency and recombination are based on several different approaches. The first approach is based on a large area illumination and local probing. Examples of this approach which are frequently used in application to PV devices include techniques such as a conductive atomic force microscopy (AFM) [21,28-33] and Kelvin probe force microscopy (KPFM) [34-37]. The other approach relies on local excitation and large area collection, with examples such as electron beam induced current [38,39] or laser beam induced current [40-42]. Photoluminescence measurements have been conducted to reveal dynamics of charge carriers and ion migration in perovskite solar cells [16,43,44]. These various techniques have their strengths and weaknesses. The implications of nanoscale measurements for device performance can be difficult to ascertain because of the difference in system geometries. The experimental geometry issues derived from contact interfaces and exposed surfaces from a macroscopic cell are largely unavoidable in nanoscale probing: in general, metal contacts hinder the access of a local probe or excitation at the desired spatial scale. Local characterization can be particularly challenging when applied to PV devices that significantly depend on the electric field or work function of contact interfaces for their operation, such as organic PVs and many types of hybrid perovskite PVs.

In this paper, we study nanoscale properties of hybrid perovskite solar cells based on methylammonium lead iodide ($MAPbI_3$). We employ a novel near-field scanning photocurrent microscopy (NSPM) technique to characterize nanoscale properties. We show changes of current collection efficiency at grain boundaries and grain interiors (GIs) caused by thermal treatment and light exposure. The critical interface between the perovskite and [6,6]-phenyl-C_{61}-butyric acid methyl ester (PCBM) driving the extraction of photoexcited electrons is mainly intact. The PCBM layer is thin enough (50 nm), as shown in Fig. 1, to access the morphology of the perovskite while remaining sufficiently conductive to transport photoexcited electrons within a few micron distances (< 2 μm) from the metal contact made of silver (Ag). We demonstrate that GBs can be either efficient carrier collection paths or additional recombination centers depending on post annealing temperatures. We suggest that the presence of a moderate amount of crystalline lead iodide (PbI_2) passivates dangling bonds at the GBs in the sample annealed at 100 °C, improving photo-generated carrier collection. In contrast, as the annealing temperature is increased to 130 °C, the GBs become major recombination centers due to an excessive amount of PbI_2 segregated at the GBs. To investigate how perovskite solar cells perform under realistic operation conditions, we determine the change of optoelectronic properties under light exposure both on the macro- and nanoscales.

2. Results and discussion

We use a novel implementation of near-field scanning photocurrent microscopy (NSPM) to measure the relative change of local photo-response in a perovskite solar cell. The device structure is as follows: indium tin oxide (ITO)/nickel oxide (NiO_x)/400-nm-thick perovskite layer ($CH_3NH_3PbI_3$ ($MAPbI_3$))/PCBM/Ag, from bottom to top (see Fig. 1). For this work, we use a tuning fork-based near-field scanning optical microscopy (NSOM) probe attached with an optical fiber. The light from a diode laser having a wavelength of 635 nm is coupled to the optical fiber as a local illumination source (see Fig. 1). The end of the optical fiber is coated with metal (Cr/Au cladding) suitable for near-field injection of light (having an aperture of 200 nm). When the light passing through the small aperture of the NSOM probe locally illuminates the sample, the photo-generated current of the sample is measured with a low-noise variable gain pre-amplifier (see the Experimental section for more detail). To achieve a high signal to noise ratio (SNR), NSPM is

performed within a few micron distances (< 2 μm) from the Ag electrode which is placed on top of the PCBM/$MAPbI_3$ layer.

Consistent with previous results [18], we can observe the appearance of PbI_2 phase in X-ray diffraction (XRD) and cross-sectional scanning electron microscopy (SEM) data (Fig. 2a and b). The peak of PbI_2 (marked with δ) along with $MAPbI_3$ peaks (marked with *) is detected in the sample annealed at moderate (100 °C) and higher temperatures (130 °C). The formation of PbI_2 is also observed in SEM images in Fig. 2b. In the SEM images of the samples annealed at 100 °C and 130 °C, distinct spots with bright contrasts are observed, which are identified as PbI_2 crystallites due to their low conductivity and increased accumulation of charge [18,47,48]. While both samples annealed at 100 °C and 130 °C have similar intensities of the PbI_2 peaks in the XRD patterns, the microscopic distribution of the PbI_2 crystallites seen in the SEM images is quite different. As shown in the black-dotted ovals in Fig. 2b, the PbI_2 phase in the sample annealed at 130 °C is frequently seen along some GBs while in the sample annealed at 100 °C the distribution of PbI_2 is relatively uniform. Note that the higher annealing temperature (130 °C) does not cause an additional decomposition and acts only as a driving force to move PbI_2 to grain boundaries.

In our previous work [45], the photovoltaic properties of the perovskite solar cells annealed at 100 °C are improved due to the conversion of the intermediate phase (MAI–PbI_2–dimethyl sulfoxide (DMSO)) into perovskite [46]. However, the performance of the cells deteriorates with further annealing in higher temperatures. Figure 2c and Table 1 show the current density (J)-voltage (V) characteristics of the two perovskite solar cells annealed at different temperatures (100 °C and 130 °C). Both J_{SC} and V_{OC} are larger by ≈ 3.8 % (21.6 mA/cm^2 vs. 20.8 mA/cm^2) and ≈ 8.7 % (0.995 V vs. 0.915 V), respectively, for the sample annealed at 100 °C. This leads to higher power conversion efficiency (η = 16.98 %) of this sample than that of the sample annealed at higher temperature (130 °C). The increase of J_{SC} in the sample annealed at 100 °C can be caused either by higher light absorption or by improved collection efficiency. The former is less likely as the two samples have similar composition according to the XRD data and therefore similar effective optical absorption. The increase of V_{OC} is more significant and cannot be accounted for by the higher J_{SC} alone. We suggest that GB defect passivation with a moderate amount of PbI_2 at GBs in the sample annealed at 100 °C leads to the improved open-circuit voltage due to the suppressed carrier recombination at GBs [18,23]. However, the distinguishable crystalline phases

of PbI_2 at GBs in the sample annealed at 130 °C are correlated with the degradation of the cell performance (see Fig. 2c and Table 1). More details on the role of PbI_2 will be discussed in the following sections.

Figure 3 shows the topography and the corresponding NSPM maps of the two perovskite cells. All NSPM maps are obtained under near-field illumination mode using a diode laser having a wavelength of 635 nm, where the intensity of the solar spectral irradiance is almost maximum. The laser injection level throughout the NSOM probe is experimentally optimized by adjusting both incident laser power and an aperture size of the NSOM probe (50 nm to 300 nm) to achieve high enough SNR without light-induced degradation on samples. The repeated line scans with the selected NSOM probe (having an aperture of 200 nm) in the same area of the fabricated sample show no light-induced degradation in the photocurrent levels (see Fig. S1 of the Supplementary material). The environmental conditions (*e.g.*, temperature and relative humidity) inside the AFM chamber where the NSPM measurement setup is configured are precisely controlled when the NSPM measurements are performed (see Fig. S2 of the Supplementary material).

The NSPM maps show strong GI to GB contrasts in the samples annealed at the two different temperatures (100 °C and 130 °C). As shown in Fig. 3b, the cell annealed at moderate temperature (100 °C) exhibits higher photocurrents at GBs than at GIs. Interestingly, an inverse photocurrent contrast is observed in the sample annealed at higher temperature (130 °C): the photocurrents at GBs are lower than those at GIs (see Fig. 3e). To better illustrate the correlation of the photocurrent distribution with the grain morphology, we overlap the topography images with the NSPM maps (see Fig. 3c and f). It is worth noting that the surface is relatively smooth, with less than 10 nm height variation over the scanned area (less than ≈ 3 % of thickness variation). However, significant variations of photocurrents (> 10 % in the sample annealed at 100 °C and up to 43 % in the sample annealed at 130 °C) in comparison with the minor topographic features are shown in the line profiles extracted from NSPM maps in Fig. 3 (see Fig. S3 of the Supplementary material). This indicates that the photocurrent contrast is not caused by surface topography and its resultant changes in light coupling or total light absorption.

To rationalize these observations, we suggest that a moderate amount of PbI_2 segregation at GBs (attained with samples annealed at 100 °C) leads to GB defect passivation, while increasing PbI_2 segregation (attained with samples annealed at 130 °C) undoes this passivation and leads to

increased GB recombination. For moderate segregation, PbI_2 possesses structural and electronic properties which facilitate GB passivation. The coordination of Pb in $MAPbI_3$ and PbI_2 is the same: in each case each Pb atom is surrounded by 6 I nearest neighbors [49]. The similar coordination environment should reduce the occurrence of dangling/wrong bonds. Electronically, bulk PbI_2 possesses a valence band offset of approximately 0.9 eV relative to bulk $MAPbI_3$ [50]. Although the band picture of electronic states does not apply at a GB interface, we may anticipate a modified local density of states at the GB in which the energy level of the highest occupied state is reduced [51]. This, in turn, lowers the hole density, so that the GB is effectively a hole barrier. Recent density functional theory calculations on GB in $MAPbI_3$ indicate that although some GB structures lack deep defect states, there are shallow hole traps at an unpassivated GB [52]. Introducing a hole barrier at the GB would therefore prevent holes from encountering these traps passivating the GB. With increasing PbI_2 segregation, the width (l) of the GB increases and may achieve a thickness which is deleterious for device performance (see black dashed ovals in Fig. 2b). For an electron-hole pair generated at the GB, the diffusion time for a hole to escape the GB is l^2/D_h, where D_h is the hole diffusion coefficient in the GB. Recombination occurs if the electron-hole pair lifetime is less than this diffusion time. For l = 50 nm, $D_h = 5 \times 10^{-6}$ m^2/s [53], recombination occurs if the lifetime is less than 0.5 ns.

The most significant shortfall of hybrid perovskite solar cells is their performance degradation under operating conditions. This degradation can be related to changes in the microscopic structure and composition. To investigate causes of the degradation, we study both macro- and nanoscale optoelectronic responses of perovskite solar cells under extended light illumination. Figure 4 shows the time dependent changes of photovoltaic properties of perovskite solar cells under continuous illumination. The macroscopic measurements are performed under Air Mass 1.5 Global (AM1.5G) 0.1 sun light (10 mW/cm^2) and ≈ 25 % relative humidity in air to avoid possible deterioration from overheating (see Fig. S2 in the Supplementary material). As seen in Fig. 4a, photovoltaic properties (the short circuit current density (J_{SC}), the open circuit voltage (V_{OC}), the fill factor (FF), and the power conversion efficiency (η)) of the sample annealed at 100 °C gradually decrease as the illumination time increases. Similar decays in V_{OC} and FF are observed for the sample annealed at 130 °C. However, the decay patterns of J_{SC} and η between the two samples are quite different (see Fig. 4 b). Despite a higher value of J_{SC} in the pristine condition of the sample annealed at 100 °C, a more drastic decay is observed after 900 min of light

illumination (down to 11.39 mA/cm^2 for 100 °C vs. 18.04 mA/cm^2 for 130 °C). Correspondingly, the drastic decrease of J_{SC} of the sample annealed at 100 °C causes significant degradation in the power conversion efficiency (from 16.98 % to 4.70 %) compared to the sample annealed at 130 °C (from 14.81 % to 7.57 %). We conclude that the sample annealed at 130 °C is more robust to the continuous light illumination than the sample annealed at a lower temperature of 100 °C.

To identify the microscopic material changes underlying or accompanying the light-induced performance degradation, X-ray diffraction peaks and cross-sectional SEM images are shown in Fig. 5. The small peaks corresponding to PbI_2 (marked with δ) at a diffraction angle of 12.75° observed in the both pristine samples annealed at 100 °C and 130 °C (similar to Fig. 2) grow as the light illumination time increases, implying the decomposition of $MAPbI_3$ into PbI_2. As described in the previous discussion, the initial distribution of PbI_2 varies by annealing temperatures, *i.e.*, PbI_2 is more evenly distributed for the sample annealed at moderate temperature (100 °C) while being concentrated at GBs for the sample annealed at higher temperature (130 °C). However, the light-induced degradation caused by the formation of PbI_2 across the perovskite layer progresses in a similar manner in both samples. After 400 min of light illumination, small voids appear within the perovskite layer, and the number of voids becomes substantial after 600 min of light illumination. The formation and evolution of voids finally cause the significant deterioration of the cell performance as shown in cross-sectional SEM images after 800 min of light illumination.

To reveal the local impact of the light-induced PbI_2 segregation, NSPM is applied for local photocurrent measurements in the multiple stages of the degradation process under continuous light illumination (AM1.5G 0.1 sun, ≈ 25 % relative humidity in air at room temperature). Figure 6 shows AFM topography images and corresponding NSPM maps for samples annealed at 100 °C (Fig. 6a-d) and 130 °C (Fig. 6e-h) taken at the specific time of light illumination. The NSPM maps taken in pristine condition, $t = 0$, are consistent with those in Fig. 3: GBs are more efficient carrier collection paths in the sample annealed at moderate temperature (100 °C) and are less efficient than GIs in the sample annealed at the higher temperature (130 °C). Interestingly, the degradation under continuous light illumination proceeds in different ways. After $t = 400$ min, the enhanced photocurrent collection at GBs is strongly suppressed in the sample annealed at 100 °C (Fig. 6c). An example of this behavior is seen at the GB marked with a white-dashed oval: the photocurrent

is significantly higher at $t = 0$ (Fig. 6b), and the photocurrent enhancement at the GB disappears after light exposure (see also Fig. S4(a) of the Supplementary material). It is worth mentioning that the decrease of carrier collection at this GB after 400 min of light illumination is not caused by the formation of voids within the perovskite layer since no severe voids are observed (inset SEM image for 400 min of light illumination in Fig. 5) despite the increased intensity of PbI_2 peak in Fig. 5. We suggest that the initial degradation of the enhanced photocurrent collection at the GBs of the sample annealed at 100 °C under illumination is caused by the dynamics of PbI_2 formation. As more structural and compositional transformation from $MAPbI_3$ to PbI_2 takes place within the perovskite layer under continuous light illumination, a large amount of PbI_2 crystallites grow at the GBs, suppressing the positive effects of GB passivation as in the area marked with the white-dashed oval in Fig. 6. This process takes place partially until 400 min of light illumination, however, it will become more widespread under continuous light illumination, rendering progressively more GBs inefficient at carrier collection. As GBs play role of dominant photocurrent collection paths for this sample, the whole performance of this sample is seriously affected by the light-induced inefficient carrier collections at GBs, resulting in rapid degradation of this sample under continuous light illumination as shown in macroscale measurements (see Fig. 4). On the contrary, the photocurrent at GBs and GIs decays at similar rate in the sample annealed at 130 °C. During the entire degradation process, the photocurrents at GIs are higher than those at GBs as carrier collections at GIs are not seriously affected by the decomposition of PbI_2 from $MAPbI_3$ under light illumination. Therefore, GIs remain as the dominant photocurrent collection paths regardless of the light illumination time in the sample annealed at 130 °C. After 800 min of light illumination, the photovoltaic properties of the sample degrade substantially (Fig. 4) and a significant amount of PbI_2 is found within the perovskite layer (Fig. 5). At this point the photocurrents reach their lowest level regardless of the annealing temperature (Fig. 6d and h). The inset SEM image in Fig. 6d shows the scanned area after 800 min of light illumination where the NSPM maps are obtained. The PbI_2 crystallite at the GB is finally released onto the surface of the sample with 800 min of light illumination, resulting in a significant cell degradation. Overall, the sample annealed at 100 °C is less stable under continuous light illumination. This is attributed to the initially optimized PbI_2 structure at GB of this sample, which is more susceptible to degradation compared to the initially sub-optimal PbI_2 GB structure of the sample annealed at 130 °C.

3. Conclusions

We analyze the structural and functional changes of hybrid perovskite solar cells caused by temperature treatments and extended light illumination processes that both drive spatially inhomogeneous material decomposition and segregation of PbI_2. A novel nanoscale measurement technique, near-field scanning photocurrent microscopy, is applied for local photocurrent measurements, which enables the observation of multiple stages of the degradation process affecting the overall efficiency of the cells. A moderate amount of PbI_2 passivates dangling bonds and unoccupied states at GBs, resulting in photocurrent enhancement at GBs compared to GIs. The higher photovoltaic performance in the perovskite solar cell annealed at 100 °C can be correlated with the nanoscale spatial pattern of photocurrent. However, the photocurrent enhancement at GBs is diminished with higher annealing temperatures or extended light exposure. The segregation of a large amount of PbI_2 at GBs hinders the photocurrent collection overcoming the positive role of the passivation. The nanoscale observation of device operation dependent on preparation and aging conditions suggests pathways to further improve the efficiency and the reliability of perovskite solar cells.

4. Experimental section

4.1. Perovskite solar cell fabrication

Prior to fabrication of the perovskite solar cells, indium tin oxide (ITO) substrates were rinsed in diluted detergent followed by sonification in water, acetone and ethyl alcohol in sequence. For formation of NiO_x thin-film, a 1 mmol of nickel(II) acetate tetrahydrate (≥ 99.0 % purity) was dissolved in 10 mL of ethyl alcohol by sonification. The prepared solution was coated on the ITO glass substrates by spin-coating at 66.7 Hz (4000 rpm) for 45 s, and the coated substrate was annealed at 300 °C for 1 h. The perovskite solution containing PbI_2 (99.99985 % purity) and methylammonium iodide (1:1 molar ratio, 0.54:1 weight ratio) in a mixture of N,N-dimethylformamide (99.8 % purity) and dimethyl sulfoxide (DMSO) (≥ 99.9 % purity) (9:1 by volume) was deposited by two step spin-coatings made at 16.7 Hz (1000 rpm) 15 s and 75 Hz (4500 rpm) for 25 s, respectively. During the second step, a droplet of diethyl ether was deposited on the substrate and soon after the substrate was transferred to a hot plate for annealing at 100 °C

and 130 °C for 10 min. Subsequently, the [6,6]-phenyl C_{61} butyric acid methyl ester ([60]PCBM, 99.5 % purity) solution (20 mg mL^{-1} in chlorobenzene) was spin-coated at 33.3 Hz (2000 rpm) for 60 s. Finally, a 120 nm-thick Ag counter electrode was deposited by thermal evaporation.

4.2. Nanoscale near-field scanning photocurrent microscopy

A tapered optical fiber (50 μm core diameter/125 μm cladding diameter) with small aperture (≈ 200 nm) in the metal coating is attached to a quartz tuning fork-based atomic force microscopy (AFM) probe. Light of a diode laser (a wavelength of 635 nm) is coupled to the optical fiber for local light injection. The perovskite solar cell is placed on a xyz piezo stage for NSPM. The topography and photocurrent were obtained simultaneously during the raster scanning made by the NSOM probe. The amplified photocurrent (with a gain of 10^7 V/A from a variable-gain low-noise current amplifier) is measured based on a lock-in technique.

4.3. Macroscale current density-voltage measurement

The current density-voltage (*J-V*) measurements were performed under AM1.5G 1 sun illumination (100 mW/cm^2) using a solar simulator.

4.4. Light illumination

To observe light-induced property changes, perovskite solar cells were continuously exposed to light up to 900 min of AM1.5G 0.1 sun illumination (10 mW/cm^2). For every 100 min of light illumination, *J-V* and NSPM measurements were performed. Other environmental factors (e.g., temperature, relative humidity in air) were controlled to isolate the effect of light illumination on devices.

Author information

*Corresponding authors.

E-mail addresses: yyoon3@ncsu.edu (Y. Yoon), dongheon.ha@nist.gov (D. Ha).

[1]These authors (Y. Yoon and D. Ha) contributed equally to this work.

Notes

The authors declare no competing financial interest.

Acknowledgements

The authors acknowledge S. M. An and G. Holland for their technical assistance. Y. Yoon and D. Ha acknowledge support under the Cooperative Research Agreement between the University of Maryland and the Center for Nanoscale Science and Technology at the National Institute of Standards and Technology, Award 70NANB14H209, through the University of Maryland.

Appendix A. Supplementary material

Supplementary material associated with this article (selecting scan area and optimizing light intensity, controlling environment during macro- and nanoscale measurements, comparison between NSPM photocurrent and AFM topography, and plan view SEM images of samples) can be found in the online version.

References

[1] NREL, Best Research-Cell Efficiencies, https://www.nrel.gov/pv/assets/images/efficiency-chart.png, (2017)

[2] M.A. Green, Y. Hishikawa, E.D. Dunlop, D.H. Levi, J. Hohl-Ebinger, A.W.Y. Ho-Baillie, Prog. Photovolt. Res. Appl. 26 (2018) 3–12.

[3] J.H. Noh, S.H. Im, J.H. Heo, T.N. Mandal, S.I. Seok, Nano Lett. 13 (2013) 1764–1769.

[4] F. Hao, C.C. Stoumpos, R.P.H. Chang, M.G. Kanatzidis, J. Am. Chem. Soc. 136 (2014), 8094–8099.

[5] G.E. Eperon, S.D. Stranks, C. Menelaou, M.B. Johnston, L.M. Herza, H.J. Snaith, Energy Environ. Sci. 7 (2014), 982–988.

[6] Z.-K. Tan, R.S. Moghaddam, M.L. Lai, P. Docampo, R. Higler, F. Deschler, M. Price, A. Sadhanala, L.M. Pazos, D. Credgington, F. Hanusch, T. Bein, H.J. Snaith, R. H. Friend, Nat. Nanotechnol. 9 (2014), 687–692.

[7] G. Li, Z.-K. Tan, D. Di, M.L. Lai, L. Jiang, J.H.-W. Lim, R.H. Friend, N.C. Greenham, Nano Lett. 15 (2015), 2640–2644.

[8] X. Hu, X. Zhang, L. Liang, J. Bao, S. Li, W. Yang, Y. Xie, Adv. Funct. Mater. 24 (2014), 7373–7380.

[9] L. Shen, Y. Fang, D. Wang, Y. Bai, Y. Deng, M. Wang, Y. Lu, J. Huang, Adv. Mater. 28 (2016), 10794–10800.

[10] Y. Fang, Q. Dong, Y. Shao, Y. Yuan, J. Huang, Nat. Photonics 9 (2015), 679–686.

[11] Y. Shao, Z. Xiao, C. Bi, Y. Yuan, J. Huang, Nat. Commun. 5 (2014), 5784.

[12] B. Wu, Y. Zhou, G. Xing, Q. Xu, H.F. Garces, A. Solanki, T.W. Goh, N.P. Padture, T.C. Sum, Adv. Funct. Mater. 27 (2017), 1604818.

[13] S. Shao, M. Abdu-Aguye, T.S. Sherkar, H.-H. Fang, S. Adjokatse, G.t. Brink, B.J. Kooi, L.J.A. Koster, M.A. Loi, Adv. Funct. Mater. 26 (2016), 8094–8102.

[14] J.-C. Blancon, W. Nie, A.J. Neukirch, G. Gupta, S. Tretiak, L. Cognet, A.D. Mohite, J.J. Crochet, Adv. Funct. Mater. 26 (2016), 4283–4292.

[15] C. Ma, K. Chen, C. Liang, C.-W. Nan, R. Ishikawa, K. More, M. Chi, Energy Environ. Sci. 7 (2014), 1638–1642.

[16] D.W. de Quilettes, S.M. Vorpahl, S.D. Stranks, H. Nagaoka, G.E. Eperon, M.E. Ziffer, H.J. Snaith, D.S. Ginger, Science 348 (2015), 683–686.

[17] R. Long, J. Liu, O.V. Prezhdo, J. Am. Chem. Soc. 138 (2016), 3884–3890.

[18] Q. Chen, H. Zhou, T.-B. Song, S. Luo, Z. Hong, H.-S. Duan, L. Dou, Y. Liu, Y. Yang, Nano Lett. 14 (2014), 4158–4163.

[19] Y. Shao, Y. Fang, T. Li, Q. Wang, Q. Dong, Y. Deng, Y. Yuan, H. Wei, M. Wang, A. Gruverman, J. Shielda, J. Huang, Energy Environ. Sci. 9 (2016), 1752–1759.

[20] D.-Y. Son, J.-W. Lee, Y.J. Choi, I.-H. Jang, S. Lee, P.J. Yoo, H. Shin, N. Ahn, M. Choi, D. Kim, N.-G. Park, Nat. Energy 1 (2016), 16081.

[21] J.S. Yun, A. Ho-Baillie, S. Huang, S.H. Woo, Y. Heo, J. Seidel, F. Huang, Y.-B. Cheng, M.A. Green, J. Phys. Chem. Lett. 6 (2015), 875–880.

[22] B. Yang, C.C. Brown, J. Huang, L. Collins, X. Sang, R.R. Unocic, S. Jesse, S.V. Kalinin, A. Belianinov, J. Jakowski, D.B. Geohegan, B.G. Sumpter, K. Xiao, O.S. Ovchinnikova, Adv. Funct. Mater. 27 (2017), 1700749.

[23] M. Zhu, W. Liu, W. Ke, S. Clark, E.B. Secor, T.-B. Song, M.G. Kanatzidis, X. Li, M.C. Hersam, J. Mater. Chem. A. 5 (2017), 24110.

[24] T. Leijtens, G.E. Eperon, S. Pathak, A. Abate, M.M. Lee, H.J. Snaith, Nat. Commun. 4 (2013), 2885.

[25] J. Berry, T. Buonassisi, D.A. Egger, G. Hodes, L. Kronik, Y.-L. Loo, I. Lubomirsky, S. R. Marder, Y. Mastai, J.S. Miller, D.B. Mitzi, Y. Paz, A.M. Rappe, I. Riess, B. Rybtchinski, O. Stafsudd, V. Stevanovic, M.F. Toney, D. Zitoun, A. Kahn, D. Ginley, D. Cahen, Adv. Mater. 27 (2015), 5102–5112.

[26] G. Niu, X. Guo, L. Wang, J. Mater. Chem. A 3 (2015), 8970–8980.

[27] D. Bryant, N. Aristidou, S. Pont, I. Sanchez-Molina, T. Chotchunangatchaval, S. Wheeler, J.R. Durranta, S.A. Haque, Energy Environ. Sci. 9 (2016), 1655–1660.

[28] J. Xu, A. Buin, A.H. Ip, W. Li, O. Voznyy, R. Comin, M. Yuan, S. Jeon, Z. Ning, J.J. McDowell, P. Kanjanaboos, J.-P. Sun, X. Lan, L.N. Quan, D.H. Kim, I.G. Hill, P. Maksymovych, E.H. Sargent, Nat. Commun. 6 (2015), 7081.

[29] J.H. Kim, P.-W. Liang, S.T. Williams, N. Cho, C.-C. Chueh, M.S. Glaz, D.S. Ginger, A.K.-Y. Jen, Adv. Mater. 27 (2015), 695–701.

[30] S.Y. Leblebici, L. Leppert, Y. Li, S.E. Reyes-Lillo, S. Wickenburg, E. Wong, J. Lee, M. Melli, D. Ziegler, D.K. Angell, D.F. Ogletree, P.D. Ashby, F.M. Toma, J.B. Neaton, I.D. Sharp, A. Weber-Bargioni, Nat. Energy 1 (2016), 16093.

[31] Y. Kutes, Y. Zhou, J.L. Bosse, J. Steffes, N.P. Padture, B.D. Huey, Nano Lett. 16 (2016), 3434–3441.

[32] J. Luria, Y. Kutes, A. Moore, L. Zhang, E.A. Stach, B.D. Huey, Nat. Energy 1 (2016), 16150.

[33] Z. Zhao, X. Chen, H. Wu, X. Wu, G. Cao, Adv. Funct. Mater. 26 (2016), 3048–3058.

[34] Bergmann, V.W. et al. Real-space observation of unbalanced charge distribution inside a perovskite-sensitized solar cell. Nature Communications 5, 5001 (2014).

[35] V.W. Bergmann, S.A.L. Weber, F.J. Ramos, M.K. Nazeeruddin, M. Grätzel, D. Li, A.L. Domanski, I. Lieberwirth, S. Ahmad, R. Berger, Nat. Commun. 6 (2015), 7269.

[36] J.L. Garrett, E.M. Tennyson, M. Hu, J. Huang, J.N. Munday, M.S. Leite, Nano Lett. 17 (2017), 2554–2560.

[37] Z. Xiao, Y. Yuan, Y. Shao, Q. Wang, Q. Dong, C. Bi, P. Sharma, A. Gruverman, J. Huang, Nat. Mater. 14 (2015), 193–198.

[38] E. Edri, S. Kirmayer, A. Henning, S. Mukhopadhyay, K. Gartsman, Y. Rosenwaks, G. Hodes, D. Cahen, Nano Lett. 14 (2014), 1000–1004.

[39] E. Edri, S. Kirmayer, S. Mukhopadhyay, K. Gartsman, G. Hodes, D. Cahen, Nat. Commun. 5 (2014), 3461.

[40] M.S. Leite, M. Abashin., H.J. Lezec, A. Gianfrancesco, A.A. Talin, N.B. Zhitenev, ACS Nano 8 (2014), 11883–11890.

[41] Y. Yoon, J. Chae, A.M. Katzenmeyer, H.P. Yoon, J. Schumacher, S. An, A. Centrone, N. Zhitenev, Nanoscale 9 (2017), 7771–7780.

[42] D. Ha, Y. Yoon, N.B. Zhitenev, Nanotechnology 29 (2018), 145401.

[43] J. You, L. Meng, T.-B. Song, T.-F. Guo, Y. Yang, W.-H. Chang, Z. Hong, H. Chen, H. Zhou, Q. Chen, Y. Liu, N. De Marco, Y, Yang, Nat. Nanotechnol. 11 (2016), 75–81.

[44] D. Moerman, G.E. Eperon, J.T. Precht, D.S. Ginger, Chem. Mater. 29 (2017), 5484–5492.

[45] I.J. Park, M.A. Park, D.H. Kim, G.D. Park, B.J. Kim, H.J. Son, M.J. Ko, D.-K. Lee, T. Park, H. Shin, N.-G. Park, H.S. Jung, J.Y. Kim, J. Phys. Chem. C 119 (2015), 27285–27290.

[46] N.J. Jeon, J.H. Noh, Y.C. Kim, W.S. Yang, S. Ryu, S.I. Seok, Nat. Mater. 13 (2014), 897–903.

[47] Y.C. Kim, N.J. Jeon, J.H. Noh, W.S. Yang, J. Seo, J.S. Yun, A. Ho-Baillie, S. Huang, M.A. Green, J. Seidel, T.K. Ahn, S.I. Seok, Adv. Energy Mater. 6 (2016), 1502104.

[48] Y. Han, S. Meyer, Y. Dkhissi, K. Weber, J.M. Pringle, U. Bach, L. Spiccia, Y.-B. Cheng, J. Mater. Chem. A 3 (2015), 8139–8147.

[49] I. Deretzis, A. Alberti, G. Pellegrino, E. Smecca, F. Giannazzo, N. Sakai, T. Miyasaka, A. La Magna, Appl. Phys. Lett. 106 (2015), 131904.

[50] D.H. Cao, C.C. Stoumpos, C.D. Malliakas, M.J. Katz, O.K. Farha, J.T. Hupp, M.G. Kanatzidis, APL Mater. 2 (2014), 091101.

[51] E. Mosconi, G. Grancini, C. Roldán-Carmona, P. Gratia, I. Zimmermann, M.K. Nazeeruddin, F. De Angelis, Chem. Mater. 28 (2016), 3612–3615.

[52] W.J. Yin, H. Chen, T. Shi, S.H. Wei, Y. Yan, Adv. Electron. Mater. 1 (2015), 1500044.

[53] R. Minder, G. Ottaviani, C. Canali, J. Phys. Chem. Solids 37 (1976), 417–424.

[54] D. Ha, C. Gong, M.S. Leite, J.N. Munday, ACS Appl. Mater. Interfaces 8 (2016), 24536–24542.

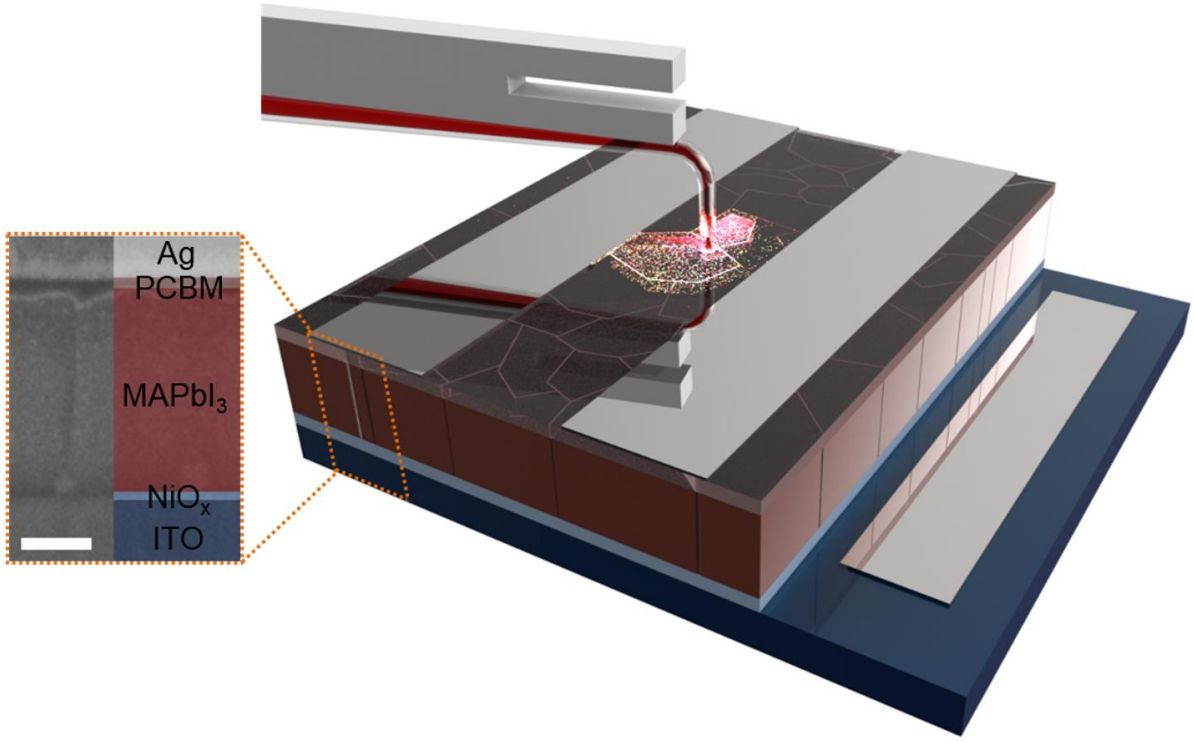

Figure 1. Schematic of NSPM technique. A tapered optical fiber with a small aperture (200 nm) in the metal coating mounted on a quartz tuning fork illuminates the sample (top of the PCBM/$CH_3NH_3PbI_3$). A SEM cross-sectional image (inset) of the perovskite cell (indium tin oxide (ITO) (280 nm)/NiO_X (15 nm)/perovskite (400 nm)/PCBM (50 nm)/Ag (120 nm), from bottom to top) shows its structure. Scale bar in the inset SEM image is 150 nm.

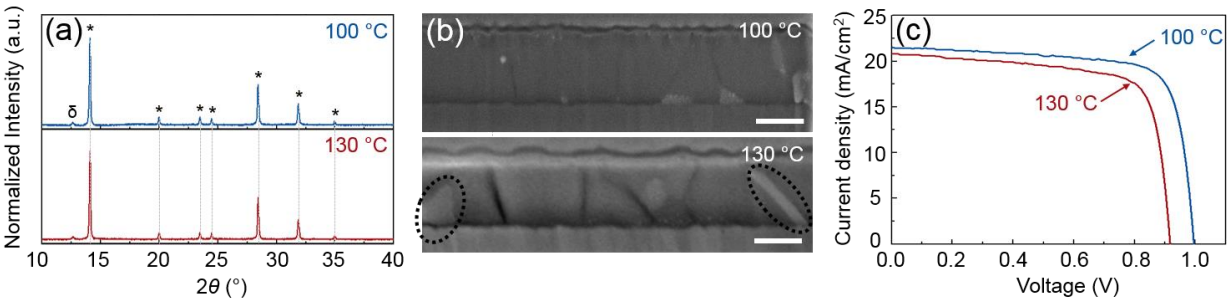

Figure 2. X-ray diffraction patterns, cross-sectional SEM images, and photovoltaic performance. (a) XRD patterns of perovskite samples annealed at two different temperatures. * and δ denote the identified diffraction peaks corresponding to the $MAPbI_3$ perovskite phase and PbI_2, respectively. (b) Cross-sectional SEM images for perovskite samples annealed at two different temperatures. Despite the similar intensity of the PbI_2 peak (*) for both samples in (b), PbI_2 (bright contrast relative to the adjacent grains) is observed mostly at grain boundaries in the sample annealed at 130 °C (see black dotted-ovals). Scale bars in (b) are 250 nm. (c) *J-V* curves of the perovskite cells (ITO/NiO_X/400-nm-thick perovskite layer/PCBM/Ag, from bottom to top) annealed at 100 °C (blue) and 130 °C (red).

Annealing temperature	J_{SC} (mA/cm^2)	V_{OC} (V)	FF (%)	η (%)
100 °C	21.60	0.995	78.4	16.98
130 °C	20.80	0.915	77.2	14.81

Table 1. Photovoltaic properties of perovskite solar cells annealed at two different temperatures (100 °C and 130 °C).

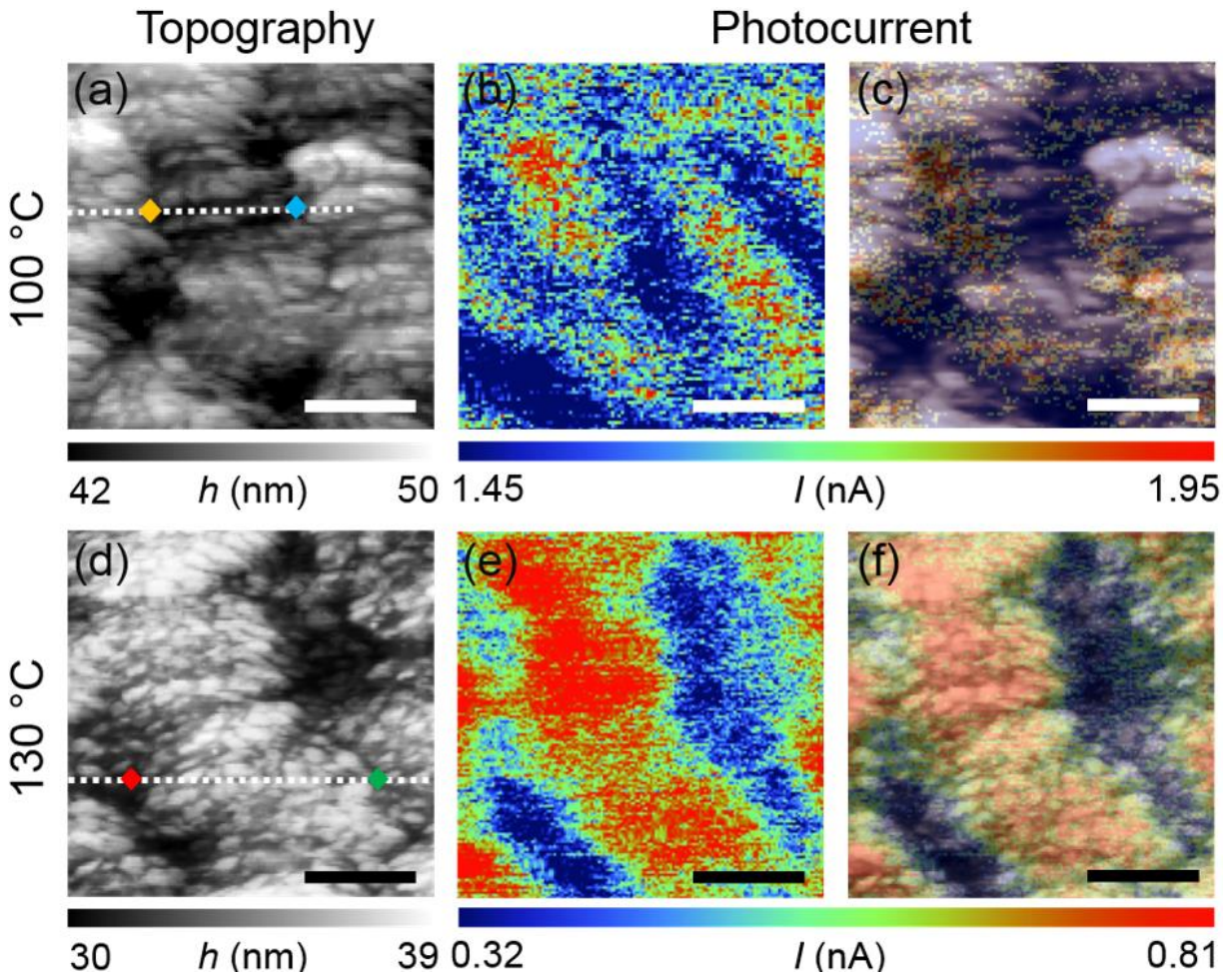

Figure 3. (a) AFM topography (*h*), (b) NSPM map (*I*), and (c) AFM topography-overlaid NSPM map of the perovskite cell annealed at 100 °C. (d) AFM topography (*h*), (e) NSPM map (*I*), and (f) AFM topography-overlaid NSPM map of the perovskite cell annealed at 130 °C. The line profiles (white-dotted lines in (a) and (d)) are reported in Fig. S3 of the Supporting Information. Scale bars in all images are 500 nm.

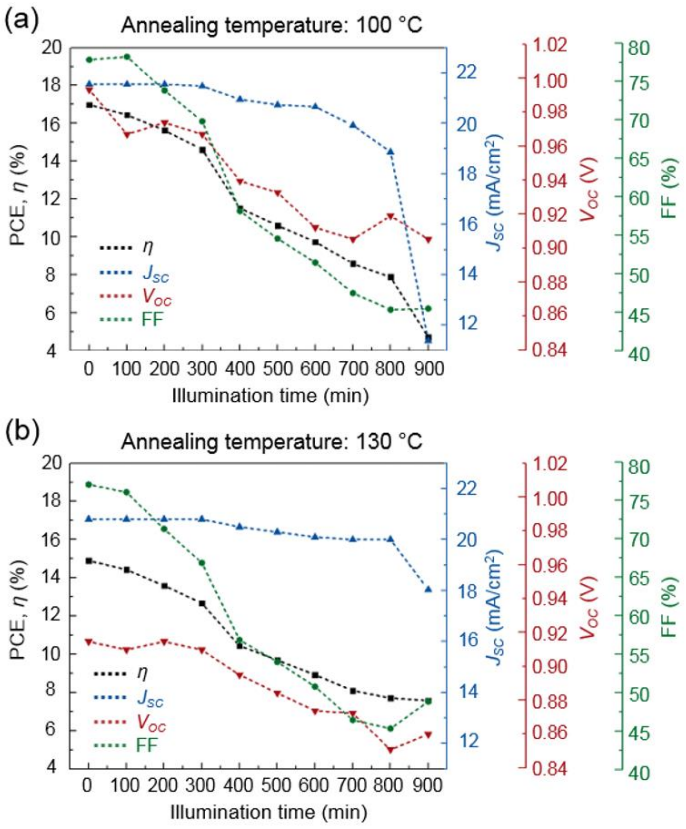

Figure 4. Light-induced effect on (a) electrical properties (η - a black dotted line, J_{SC} - a blue dotted line, V_{OC} - a red dotted line, and FF - a green dotted line) of the perovskite solar cell annealed at 100 °C under continuous AM1.5G 0.1 sun light illumination. Light-induced effect on (b) electrical properties for the sample annealed at 130 °C under the same illumination condition: AM 1.5G 0.1 sun, relative humidity ≈ 25% at room temperature in air. Estimated error in the measurements is < 1 % [54].

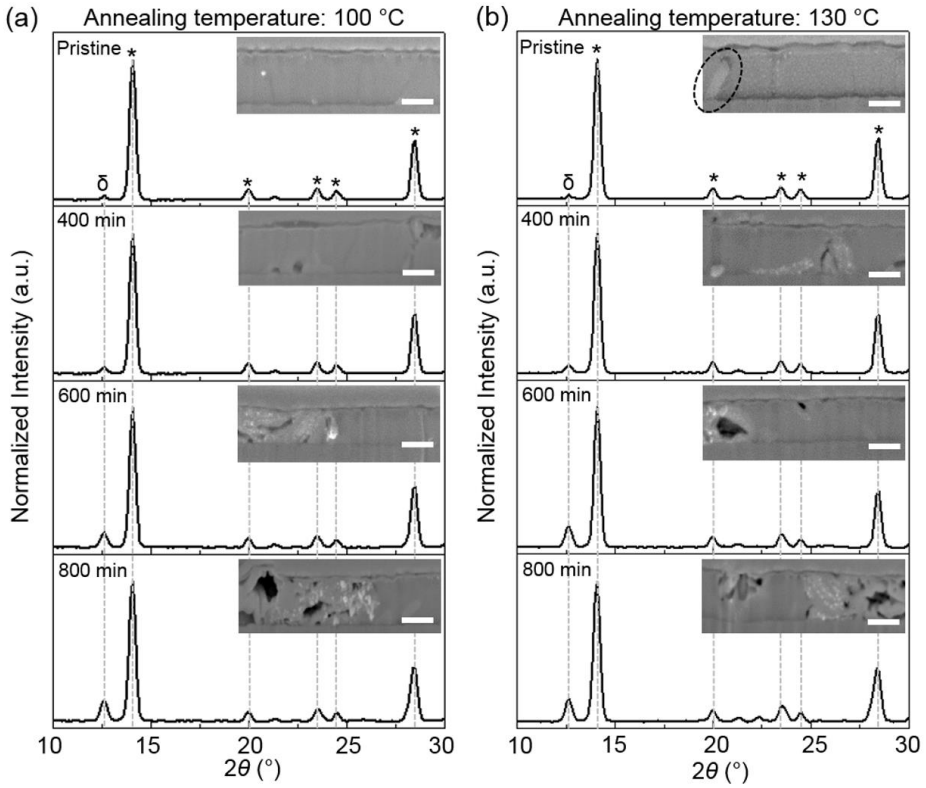

Figure 5. X-ray diffraction patterns with respect to the light exposure time for the samples annealed at (a) 100 °C and (b) 130 °C, respectively. δ and * indicates PbI_2 and $MAPbI_3$, respectively. As the exposure time increases, more compositional and/or structural conversion from $MAPbI_3$ to PbI_2 is observed for both samples. Insets: scanning electron microscopy (SEM) images show corresponding cross-sectional views of the samples for the corresponding exposure time. Black-dotted oval in the inset SEM for the sample annealed at 130 °C shows excess of PbI_2 agglomerated at a grain boundary. Scale bars in all inset SEM images are 250 nm.

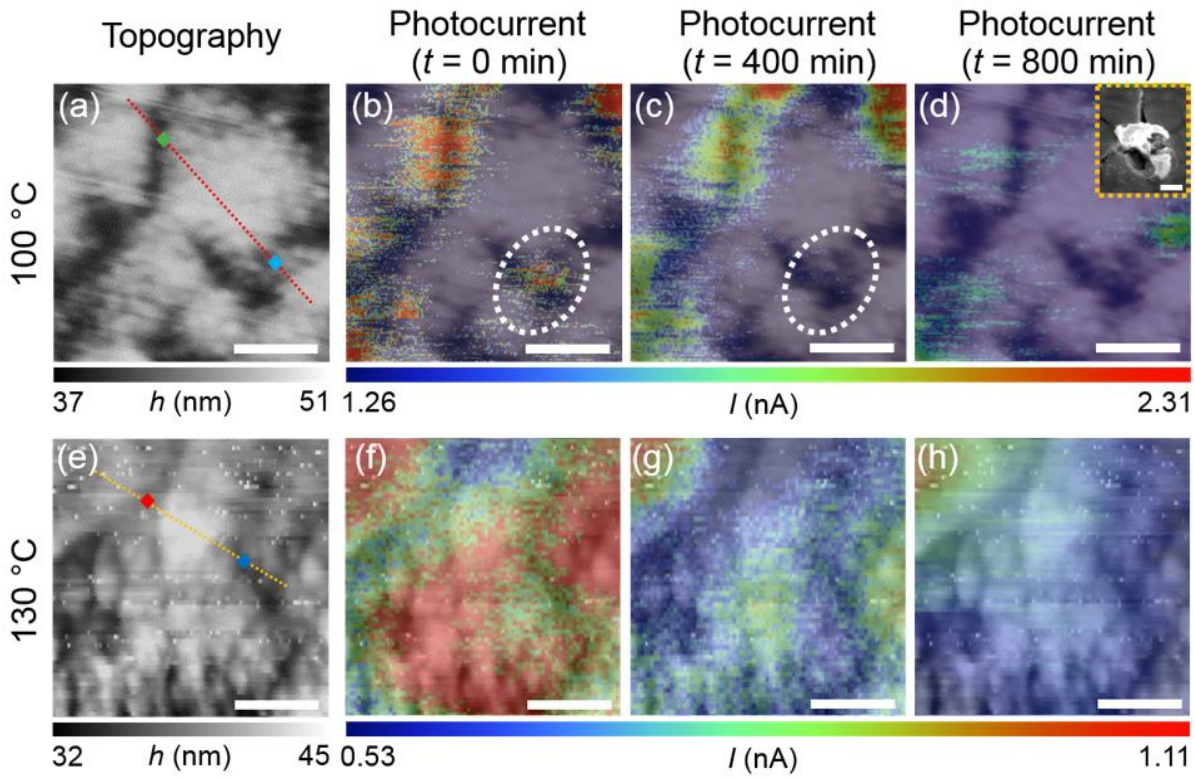

Figure 6. (a) AFM topography (*h*) and the corresponding NSPM maps (*I*) for the sample annealed at 100 °C measured simultaneously: (b) at pristine condition, (c) after 400 min and (d) 800 min of light exposure. (e) AFM topography (*h*) and NSPM maps (*I*) are measured for the sample annealed at 130 °C with different time of light exposure: (f) pristine, (g) 400 min, and (h) 800 min. For both samples, NSPM maps are made on the same area. Inset: SEM image in (d) shows the same area where AFM scanning is made after aging the sample under 800 min of light illumination. Scale bars in all images including the inset SEM image are 500 nm.